

The continuum and narrow line region of the NLS1 galaxy Mrk 766

A. Rodríguez-Ardila^{1*}, M. Contini², S. M. Viegas³

¹ Laboratório Nacional de Astrofísica - Rua dos Estados Unidos 154, Bairro das Nacões. CEP 37504-364, Itajubá, MG, Brazil

² School of Physics and Astronomy, Tel Aviv University, Tel Aviv 69978, Israel

³ Instituto de Astronomia, Geofísica e Ciências Atmosféricas - USP, Rua do Matão 1226, 05508-900 So Paulo SP, Brazil

Accepted in MNRAS

ABSTRACT

We present the first spectroscopic observations in the interval $0.8\mu\text{m}$ – $4.0\mu\text{m}$, complemented with existing *HST* UV and optical spectroscopy, of the narrow-line Seyfert 1 galaxy Mrk 766. The NIR spectrum is characterized by numerous permitted lines of H I, He I, He II and Fe II, and forbidden lines of [S II], [S III] and [Fe II] among others. High ionized species such as [Si IX], [Si X], [S IX] and [Mg VII] are also observed. The continuum emission has a complex shape, with contribution of the central engine, circumnuclear stellar population and dust. This last component is evidenced by the presence of an excess of emission peaking at $2.25\mu\text{m}$, well fitted by blackbody function with $T_{\text{bb}}=1200$ K. That temperature is close to the evaporation temperature of graphite grains. As such, it provides strong evidence of hot dust, probably very close to the nucleus. Consistent modeling of the line spectrum and the broad band continuum by composite models, which account for the photoionizing flux of the central engine and shocks, shows that shock velocities range between 100 and 500 km s^{-1} , the preshock densities between 100 and 1000 cm^{-3} and the radiation fluxes from the active centre between 10^9 and $5\text{ }10^{12}\text{ photons cm}^{-2}\text{ s}^{-1}\text{ eV}^{-1}$ at 1 Ryd with spectral indices $\alpha_{UV} = -1.5$ and $\alpha_X = -0.4$. Adopting silicate grains, dust-to-gas ratios are between 10^{-6} and $4\text{ }10^{-4}$ by mass. The emitting clouds are at an average distance of 160 pc from the centre, with high velocity clouds closer and low velocity clouds farther from the centre. The N/H relative abundance deduced from the fit of the [N II] 6548+/[O III] 5007+ line ratio could be twice solar. On the other hand, Fe is depleted from the gaseous phase by a factor > 2 , most probably trapped into grains. Ratios of calculated to observed line ratios to $\text{H}\beta$ indicate an average contribution of the broad line region to the observed $\text{H}\beta$ of about 40%.

Key words: galaxies: active – galaxies: nuclei – galaxies: Seyfert – radio: galaxies

1 INTRODUCTION

A large amount of information about the structure and physical conditions of active galactic nuclei (AGN) has been obtained during the last decade from the analysis of their optical emission-line spectrum (see the review of Véron-Cetty & Véron 2000 and references therein). More recently, spectroscopic observations in the near- and mid-infrared have been added to that of the optical with enough resolution to reveal important aspects from both the narrow line and broad line regions (NLR and BLR, respectively; Sosa-Brito et al. 2001; Knop et al. 2001; Rodríguez-Ardila et al. 2002a,b) as well as from the circumnuclear environment (Thornley et al. 2000; Lutz et al. 2003; Verma et al. 2003). Given that the infrared re-

gion is substantially less affected by extinction, it also allows one to probe depths unreachable with data at shorter wavelengths (Sosa-Brito et al. 2001; Nagar et al. 2002).

Among the different types of active galaxies, the narrow-line Seyfert 1 class (NLS1, Osterbrock & Pogge 1985) are special targets because they share all optical properties of the Seyfert 1s except the very narrow Balmer lines ($\text{FWHM} < 2000\text{ km s}^{-1}$, by definition) and the strong optical Fe II emission. In the X-rays region, NLS1 are also peculiar because of the soft X-rays excess above the hard X-rays power-law extrapolation that dominates below 1 keV (Puchnarewicz et al. 1992; Boller et al. 1996) and the very steep soft photon spectral index (Leighly 1999b). These extreme properties could derive from the fact of NLS1 being sources with relatively small black hole masses ($M_{\text{BH}} \sim 10^{6-7} M_{\odot}$) and high Eddington ratios $L/L_{\text{edd}} \sim 1-10$ (e.g. Boroson (2002); Grupe (2004)).

In the near-infrared (NIR), NLS1 usually present a rich emission-line spectrum (Rodríguez-Ardila et al. 2002a,b; Grupe & Thomas 2002). In addition, features associated to the

* Visiting Astronomer at the Infrared Telescope Facility, which is operated by the University of Hawaii under Cooperative Agreement no. NCC 5-538 with the National Aeronautics and Space Administration, Office of Space Science, Planetary Astronomy Program.

BLR such as the Fe II and the permitted H I lines, strongly blended in classical Seyfert 1 (Sy 1), are easily separated in NLS1 because of the narrowness of their BLR lines and the larger separation in wavelength between the individual features. This, in turn, favors the analysis of the forbidden line spectrum. Weak features, usually lost amid strongly blended BLR lines in the optical region, are more easily seen in the NIR spectrum. It is then interesting to study the cases where the NLR lines are conspicuous in order to examine the physical conditions of the emitting gas and the continuum properties to construct a coherent picture that explains the parameters driving the emission of the NLR in NLS1.

With the above in mind, a program to consistently study a selected sample of NLS1 galaxies, with emphasis on the NIR information, was started with Ark 564 (Contini et al. 2003a; hereafter Paper I). In this work, a similar analysis is applied to the NLS1 galaxy Mrk 766 (=NGC 4253). Located at $z = 0.0129$, it is classified as a barred SBa galaxy with optical overall orientation P.A.=69° (MacKenty 1990). HST images of this object show filaments, wisps and irregular dust lanes around an unresolved nucleus (Malkan et al. 1998). Radio observations at 3.6 cm, 6 cm and 20 cm (Ulvestad et al. 1995; Nagar et al. 1999) show that the radio source appears to be extended in both P.A. $\sim 27^\circ$ (on a scale of $0''.25$) and P.A. 160° (on a scale of $0''.3$, Nagar et al. 1999). In the optical, the emission is extended (González Delgado & Pérez 1996; Mulchaey et al. 1996) through a region of total size greater than that of the radio source.

In X-rays, Mrk 766 is variable on a few hours time-scale and presents a strong soft X-ray excess (Molendi et al. 1993; Leighly 1996; Mason et al. 2003). Boller et al. (1996) report one of the flattest *ROSAT* soft X-ray photon spectral index for Mrk 766 ($\alpha_X = -1.5$) in their sample of NLS1 galaxies, yet steeper than what most broad line Seyfert 1 or even some other NLS1 show. Grupe et al. (2001) give a $\alpha_X = -1.77$ for this source, which is exactly the mean value for the whole sample of soft X-ray selected AGN reported in Grupe (2004), not as flat as initially found. Nandra et al. (1997) reported the detection of an Fe K α line in the X-ray spectrum. Moreover, recent *XMM-Newton* observations have caused a debate over whether or not the soft X-ray spectrum arises from a dusty warm absorber or relativistic emission lines (Mason et al. 2003).

In the ultraviolet, the spectrum of Mrk 766 looks also unusual among Seyfert 1 galaxies due to the weakness of both the ultraviolet continuum and big blue bump (Walter & Fink 1993). The deficit of ultraviolet photons has been attributed to reddening (Page et al. 1999) and/or to absorption (Walter & Fink 1993). Actually, Walter & Fink (1993) claim that there is no basic difference between the unabsorbed optical to X-ray continua emitted by Mrk 766 and by other Seyfert 1 galaxies. The dusty scenario is supported by the optical polarization of Mrk 766, of ~ 2 per cent increasing to the blue, due to scattering by dust grains. The grains are probably located within the narrow line region given that the broad lines show more polarization than the narrow lines (Goodrich 1989).

In the near-infrared, much of the information available for Mrk 766 comes from imaging studies. Alonso-Herrero et al. (1998) report that the surface brightness of this source at the 0.5–1 kpc radius is 1–2 mag arcsec $^{-2}$ brighter than that of normal galaxies. Moreover, it shows one of the reddest *H-K* colours for the 0.5 and 1 kpc diameter apertures of their sample. This result is confirmed by the *J*- and *K'*-band imaging work of Márquez et al. (1999), where it is shown that Mrk 766 displays a double nuclear structure with a (*J-K'*) color index redder than the rest of the galaxy. That structure seems to correspond to a feature delineated by the

dust pattern that surrounds the innermost $2''$ in the HST optical image (Malkan et al. 1998). Spectroscopically, Mrk 766 have been poorly studied in this band. To our knowledge, the only observations of Mrk 766 published in the NIR region is the *K*-band spectroscopy of Grupe & Thomas (2002) and the *L*-band spectroscopy of Rodríguez-Ardila & Viegas (2003). In the former, the spectrum clearly reveals Br γ and probably the H $_2$ and [Si VI] lines. In the later, the $3.3\mu\text{m}$ emission, attributed to polycyclic aromatic hydrocarbons (PAH), is detected. The observation of PAH emission is usually taken as unambiguous evidence of starburst activity. Interestingly, a strong starburst might be behind the high [O III]/H β ratio observed in Mrk 766, so extreme (Grupe 2004) as to possibly exclude Mrk 766 from the NLS1 class, following the definition of NLS1s by Osterbrock & Pogge (1985).

For all the above, Mrk 766 arises as a very interesting target to continue our analysis of the continuum and NLR properties of NLS1 galaxies. To this purpose, NIR observations supplemented with archival UV - optical and mid-far infrared data will be used in this work. This set of data is described in Sec. 2. The description and characterization of the observed NIR continuum is described in Sec. 3. A discussion about the most important emission line features detected in the spectrum, both from the BLR and NLR, is presented in Sec. 4. In a first approach to apprehend the nature of Mrk 766, we compare its SED with that of NLS1 galaxies (Sec. 5), and, particularly, with the SED of Ark 564, which has been already modeled (Paper I). This step will help at constraining the models for the evaluation of the emission-line ratios presented in Sec. 6. After modeling the emission-line spectrum, the associated (and consistent) SED of the continuum is discussed in Sec. 7. The concluding remarks appear in Sec. 8.

2 OBSERVATIONS

NIR spectra of Mrk 766 in the interval 0.8–2.4 μm were obtained at the NASA 3 m Infrared Telescope Facility (IRTF) on the nights of April 21 and 25, 2002 (UT) using the SpeX spectrometer (Rayner et al. 2003). In addition, spectra covering the interval 3–4 μm were also obtained with the same setup on the night of April 22 (UT). In both cases, the detector consisted of a 1024×1024 AL-ADDIN 3 InSb array with a spatial scale of $0.15''/\text{pixel}$. Simultaneous wavelength coverage was obtained by means of prism cross-dispersers. A $0''.8 \times 15''$ slit, oriented at the PA of 112° , was used during the observations. The resulting spectral resolution was 360 km s^{-1} for both setups. The observations were done nodding in an ABBA source pattern with individual integration times of 120 s and 30 s for the short (0.8–2.4 μm) and long (3–4 μm) wavelength range, respectively. The total on-source integration time was 1680 s and 1080 s for the April 21 and 25, respectively, and 900 s for the 22 April observation. The A0 V star HD79108 ($V=6.13$) was observed after the target's to remove the telluric bands. It was also used to flux calibrate the spectra. The spectra were reduced following standard procedures for NIR spectroscopy. They include subtracting consecutive 2-D AB pairs to remove background, flat fielding the resulting imaging, extracting the signal along the dispersion axis, co-adding and calibrating. The signal within the central $0''.8 \times 1''$ was summed up to obtain the nuclear spectrum. The $1''$ extraction window along the slit, with centre at the peak continuum luminosity in K, is in accord to the seeing of $0''.8$ measured during the observations. This window size corresponds to the inner 250 pc ($H_0=75 \text{ km s}^{-1} \text{ Mpc}^{-1}$) of the AGN. No effort to extract information from the extended emission, seen up to ~ 400 pc

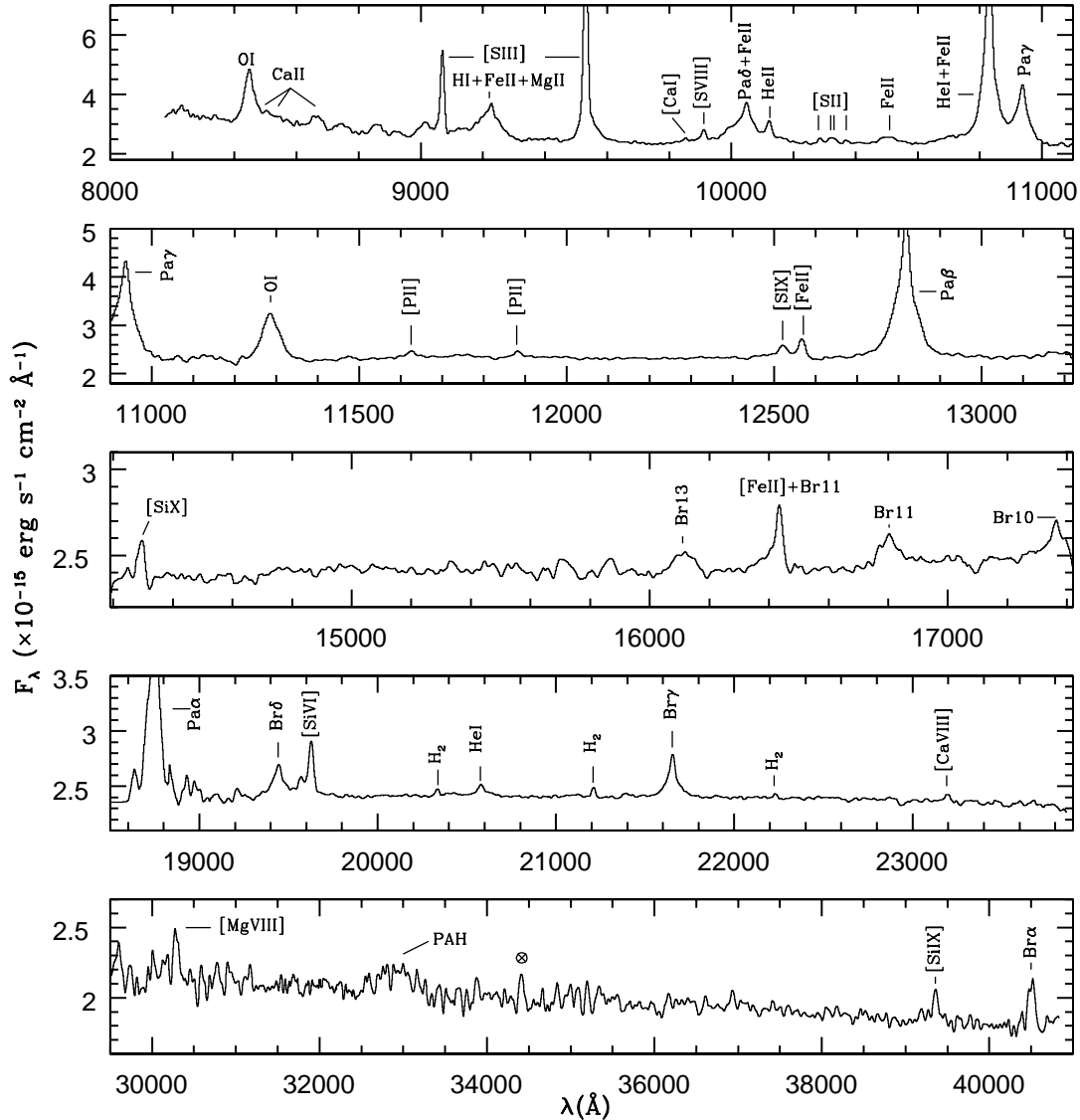


Figure 1. Observed NIR spectrum of Mrk 766 in laboratory wavelengths. In order to easy the identification of the spectral features, the most important permitted and forbidden lines are marked.

NW and SE of the centre, was done. The reduction and extraction procedures were done using the in-house software Spextool (Cushing et al. 2004) provided by the IRTF observatory. For telluric band correction and flux calibration, a script also provided by IRTF, designed to this purpose (Vacca et al. 2003) was employed. Afterward, the two spectra in the short wavelength range were averaged to form a single 0.8–2.4 spectrum.

Figure 1 show the final rest-frame NIR spectrum of Mrk 766. Note that within the intervals $1.74 \mu\text{m}$ – $1.86 \mu\text{m}$ and $2.4 \mu\text{m}$ – $2.9 \mu\text{m}$, the atmospheric transmission drops to zero. For this reason, these two regions are missing in Figure 1. As can be seen, the spectrum is dominated by permitted emission lines of H I, He I, O I and Fe II. Also prominent are the forbidden lines of [S III] $\lambda\lambda 9068, 9531$, [Si VI] $1.963 \mu\text{m}$, [Mg VIII] $3.03 \mu\text{m}$ and [Si IX] $3.936 \mu\text{m}$. Note also the bump centred at $3.3 \mu\text{m}$, attributed to emission of PAH molecules (Rodríguez-Ardila & Viegas 2003). It represents an unambiguous signature of starburst activity within the central 250 pc of this NLS1 galaxy.

Fluxes of the identified NIR lines measured from our spectrum are listed in Table 1. They were calculated by fitting a Gaussian to the observed profile and then integrating the flux under the curve. The LINER software (Pogge & Owen 1993) was used for this purpose.

Archival *HST* data taken with the Space Telescope Imaging Spectrograph (STIS) on 11 April 2000 (UT) were also used in order to measure the flux of the most important UV lines of Mrk 766. The spectra were obtained through the $52'' \times 0.2''$ slit and the low-resolution ($R \sim 750$) G140L and G230L gratings. The spectra cover the rest-frame wavelength range 1100–1690 Å and 1550–3200 Å, respectively. The final rectified wavelength calibrated x2d spectrum produced by the *HST* pipeline was used to extract the 1-D spectrum. The extraction window in the spatial direction was the same used in the NIR data. The IRAF package was used to this purpose.

In the optical region, fluxes for the most important lines were taken from González Delgado & Pérez (1996) (hereafter, GP96). They report relatively strong Fe II emission and coronal lines, as

well as extended optical emission through a region the total size of 8" (about 2 kpc) along the stellar bar. Because of the high quality of the data and resolution, that matches ours', the nuclear fluxes of GP96 will be used through this work.

Finally, the fluxes of the emission lines from UV to NIR were dereddened for Galactic and internal extinction. The value of $E(B-V)$ corresponding to our Galaxy is 0.02 (Schlegel et al. 1998). The internal extinction $E(B-V)=0.5\pm 0.1$, applied to the data, was determined from the average of the extinction values derived from the flux ratio of the narrow components of $\text{Pa}\beta/\text{Pa}\gamma$, $E(B-V)=0.69$, and that determined by GP96 [$E(B-V)=0.38$]. The value found from the Paschen lines agrees with that derived from the Balmer decrement (Grupe et al. 1998), indicating that Mrk 766 is indeed highly reddened in the optical/UV. Note that higher values of extinction were also found, for example, from the flux ratios $[\text{Fe II}] 1.257\mu\text{m}/1.644\mu\text{m}$ [$E(B-V)=1.2$] and $\text{Br}\gamma/\text{Pa}\beta$ [$E(B-V)=1.15$]. However, we rejected the latter two values because it is not certain if the bulk of the NLR gas is affected by such large values of extinction, mainly if we take into account that the optical spectrum of Mrk 766 displays prominent $[\text{Ne V}] 3346, 3426 \text{ \AA}$ lines (see Figure 3 of GP96), which are located in the blue end of the spectrum. Table 2 list the dereddened optical and NIR narrow line fluxes. Note that the extinction law of Cardelli et al. (1989) was applied in that correction.

The choice of the Cardelli et al. (1989) extinction law is due to the fact that we are assuming that the dust affecting the NLR is located in a non-nuclear environment. It is yet possible that the observed continuum in the UV-optical region is affected by the same amount of extinction, but if there is an additional nuclear dust component, it is likely that the Cardelli et al. (1989) law is no longer valid. The main support to this is the lack of the $\lambda 2175$ dip in the UV continuum shape. This is in accord to recent claims by Gaskell et al. (2004), who provided substantial evidence of a relative lack of small grains in the nuclear dust, which would explain the absence of the $\lambda 2175$ dip in most AGN spectra. They proposed a reddening curve fairly universal, being quite flat in the UV but selective in the optical. Due to the lack of enough continuum points in the optical region that adequately connects the NIR with the *HST* data, we feel that any correction to the nuclear UV continuum is highly uncertain. Since our interest is concentrated in the NLR gas and the reprocessed continuum by this gas, we feel that this correction does not affect our main results and conclusions.

3 THE NIR CONTINUUM

3.1 The observed continuum

The continuum emission displayed by Mrk 766 in the interval $0.8-4 \mu\text{m}$ is complex (see Figure 2). At least three main features can be easily identified in its spectrum: (i) a steep continuum blueward of $1 \mu\text{m}$, very similar to the so-called small blue bump in the optical region observed in AGN around 4000 \AA ; (ii) a turnover of the continuum at $\sim 1.1 \mu\text{m}$. The continuum emission raises longward up to $\sim 2.2 \mu\text{m}$, where it reaches a maximum; (iii) a steep decline of the continuum flux with wavelength, longward of $2.2 \mu\text{m}$.

Few AGN at a similar wavelength coverage and spectral resolution in the NIR region are available in the literature, so a meaningful comparison of the continuum observed in Mrk 766 with that of other AGN is not possible. However, data published for the NLS1s galaxies IZw 1 (Rudy et al. 2000), Mrk 478 (Rudy et al. 2001) and Ark 564, Ton S 180, 1H 1934-063 and

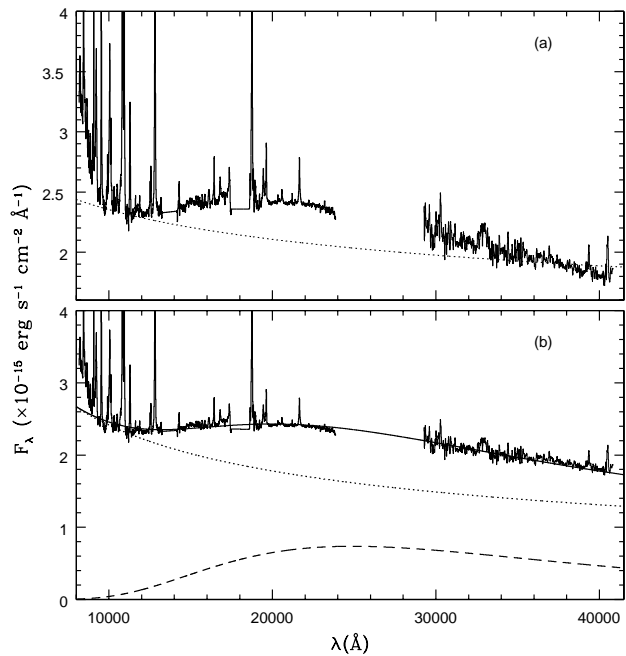


Figure 2. (a) NIR SED observed in Mrk 766. The dotted line is best-fitted power-law function. Note the strong excess of emission over the power-law, in the interval $12000-32000 \text{ \AA}$. Note also that the power-law overpredicts the continuum emission longward of 38000 \AA . (b) NIR SED modeled with a composite function: a power-law (dotted lines), of spectral index $\alpha=-0.44$, as found by Alonso-Herrero et al. (2003), plus a blackbody distribution (dashed line) of $T_{\text{bb}}=1200 \text{ K}$. The thick line represent the sum of both components.

Mrk 1044 (Rodríguez-Ardila et al. 2002a) show that the turnover of the continuum near $1.1 \mu\text{m}$ is a common feature and may represent the shift from the non-thermal continuum emitted by the active nucleus to the stellar and thermal dust emission from the circumnuclear region that dominates at longer wavelengths. The rapid rise of the continuum in the J and H bands with a peak at the K-band, and then its slow decline, has not been reported before, to our knowledge, for an AGN but IZw 1. Note, however, that the IZw 1 spectrum of Rudy et al. (2000) ends at $2.40 \mu\text{m}$.

In order to characterize the NIR continuum emission in Mrk 766, a power-law of the form $F_{\lambda} \propto \lambda^{\alpha}$ was fitted to the data. The task *nfit1d* of the STSDAS package of IRAF was used to this purpose. Special care was taken to not include emission lines in the spectral windows used in the fit. The result is shown in the upper panel of Figure 2. The derived spectral index α was -0.16 , significantly flatter than the average value of -0.64 found for the AGN sample of Edelson & Malkan (1986) and also flatter than the value of -0.44 found by Alonso-Herrero et al. (2003) in the interval $1-16 \mu\text{m}$ for Mrk 766. It can be seen from Fig. 2 that the fitted function overpredicts the continuum emission redward of $4 \mu\text{m}$. In addition, it shows that a single power-law cannot describe the continuum emission in the $1-4 \mu\text{m}$ region. There is an excess of emission over the power-law that in no way follows a simple function.

A closer look to the overall shape of the excess of emission over the power-law, in the wavelength range $1-4 \mu\text{m}$, suggests that it approaches to that of a blackbody distribution. In order to test this hypothesis, we fitted a composite function (power-law plus blackbody) to the observed NIR SED. In the fit, the spectral index of the power-law was constrained to the value $\alpha=-0.44$, found by

Table 1. Observed NIR emission line fluxes measured in Mrk 766

Line	Flux $\times 10^{-15}$ erg cm^{-2} s^{-1}	Line	Flux $\times 10^{-15}$ erg cm^{-2} s^{-1}
Br α 4.052 μm	31.3 \pm 4.70	HeII (b*) 1.162 μm	2.94 \pm 0.81
[SiIX] 3.935 μm	17.06 \pm 3.60	[P1I] 1.146 μm	1.44 \pm 0.29
[MgVIII] 3.027 μm	26.6 \pm 8.06	O1 1.128 μm	48.86 \pm 2.40
[CaVIII] 2.321 μm	2.47 \pm 0.60	Pa γ (n*) 1.937 μm	13.05 \pm 0.77
H ₂ 2.223 μm	0.81 \pm 0.15	Pa γ (b*) 1.937 μm	87.30 \pm 3.07
Br γ (n*) 2.157 μm	7.40 \pm 0.35	FeII 1.086 μm	50.6 \pm 2.40
Br γ (b*) 2.157 μm	20.0 \pm 2.26	HeI 1.083 μm	216.4 \pm 1.53
H ₂ 2.121 μm	2.36 \pm 0.24	FeII 1.050 μm	14.86 \pm 1.96
HeI (n*) 2.058 μm	2.03 \pm 0.20	[SiI] 1.037 μm	1.67 \pm 0.46
HeI (b*) 2.058 μm	6.09 \pm 1.10	[SiI] 1.033 μm	2.11 \pm 0.46
H ₂ 2.033 μm	1.73 \pm 0.22	[SiI] 1.032 μm	3.38 \pm 0.46
[SiVI] 1.963 μm	15.6 \pm 0.94	[SiI] 1.028 μm	2.91 \pm 0.46
H ₂ 1.957 μm	4.39 \pm 0.39	FeII 1.017 μm	6.23 \pm 2.10
[FeII] 1.634 μm	8.20 \pm 0.40	HeII (n*) 1.012 μm	18.57 \pm 2.02
[SiX] 1.430 μm	6.47 \pm 0.54	HeII (b*) 1.012 μm	5.68 \pm 0.70
Pa β (n*) 1.281 μm	27.15 \pm 0.50	Pa δ (n*) 1.004 μm	4.82 \pm 0.69
Pa β (b*) 1.281 μm	117.8 \pm 1.80	Pa δ (b*) 1.004 μm	68.7 \pm 2.7
[FeII] 1.257 μm	7.69 \pm 0.70	FeII 0.999 μm	21.98 \pm 2.13
[SiX] 1.252 μm	9.42 \pm 0.96	[SVIII] 0.991 μm	10.0 \pm 1.00
[P1I] 1.188 μm	2.19 \pm 0.29	[CaI] 0.985 μm	5.90 \pm 1.34
HeII (n*) 1.162 μm	1.40 \pm 0.24	[SiII] 0.953 μm	110.0 \pm 0.90

n and *b* stand for the narrow and broad components, respectively, of the permitted emission lines.

Table 2. Line fluxes in Mrk 766 corrected for E(B-V)=0.5 and normalized to $F_{5007+} \times 100$

Line	Flux 10^{-14} erg cm^{-2} s^{-1}	F_{λ}/F_{5007}	Line	Flux 10^{-14} erg cm^{-2} s^{-1}	F_{λ}/F_{5007}
[SiIX] 3.935 μm	1.87 \pm 0.39	1.10 \pm 0.25	[SiII] 6717 Å	4.14 \pm 0.33	2.45 \pm 0.26
[MgVIII] 3.027 μm	2.94 \pm 0.88	1.74 \pm 0.54	HeI 6678 Å	2.00 \pm 0.22	1.18 \pm 0.16
[CaVIII] 2.321 μm	0.30 \pm 0.07	0.17 \pm 0.04	[NII] 6584 Å	18.01 \pm 1.08	10.66 \pm 0.99
HeI 2.058 μm	0.96 \pm 0.13	0.57 \pm 0.09	H α 6563 Å	281.1 \pm 16.9	166.3 \pm 15.5
[SiVI] 1.963 μm	1.87 \pm 0.11	1.11 \pm 0.10	[NII] 6548 Å	4.00 \pm 0.12	2.37 \pm 0.18
[FeII] 1.634 μm	1.05 \pm 0.05	0.62 \pm 0.05	FeX 6375 Å	0.45:	0.27 \pm 0.02
[SiX] 1.430 μm	0.91 \pm 0.07	0.54 \pm 0.06	[OI] 6363 Å	1.28 \pm 0.12	0.76 \pm 0.09
Pa β 1.281 μm	21.34 \pm 0.21	12.63 \pm 0.91	[OI] 6300 Å	2.80 \pm 0.22	1.66 \pm 0.18
[FeII] 1.257 μm	1.12 \pm 0.10	0.66 \pm 0.08	[FeVII] 6086 Å	2.40 \pm 0.12	1.42 \pm 0.12
[SiX] 1.252 μm	1.33 \pm 0.13	0.79 \pm 0.10	HeI 5876 Å	13.74 \pm 1.10	8.13 \pm 0.87
[P1I] 1.188 μm	0.35 \pm 0.05	0.21 \pm 0.03	[NII] 5755 Å	0.37 \pm 0.06	0.22 \pm 0.04
HeII 1.162 μm	0.68 \pm 0.13	0.40 \pm 0.08	[FeVII] 5721 Å	1.33 \pm 0.12	0.79 \pm 0.09
[P1I] 1.146 μm	0.23 \pm 0.05	0.13 \pm 0.03	[OI] 5577 Å	0.33 \pm 0.07	0.20 \pm 0.04
Pa γ 1.937 μm	12.27 \pm 0.37	7.26 \pm 0.56	[OIII] 5007 Å	169.3 \pm 11.9	100.0 \pm 7.10
HeI 1.083 μm	36.02 \pm 0.36	21.31 \pm 1.53	H β 4861 Å	82.93 \pm 2.95	49.4.
[SiII] 1.037 μm	0.29 \pm 0.08	0.17 \pm 0.05	[ArVI] 4740 Å	0.67 \pm 0.09	0.39 \pm 0.06
[SiI] 1.033 μm	0.36 \pm 0.08	0.21 \pm 0.05	[ArVI] 4711 Å	0.63 \pm 0.09	0.37 \pm 0.06
[SiI] 1.032 μm	0.57 \pm 0.08	0.34 \pm 0.05	HeII 4686 Å	7.34 \pm 0.51	4.34 \pm 0.43
[SiI] 1.028 μm	0.53 \pm 0.09	0.32 \pm 0.06	[OIII] 4363 Å	3.47 \pm 0.59	2.05 \pm 0.38
HeII 1.012 μm	4.27 \pm 0.38	2.53 \pm 0.29	H γ 4341 Å	34.82 \pm 3.13	20.6 \pm 2.36
Pa δ 1.004 μm	12.94 \pm 0.52	7.66 \pm 0.62	[SiII] 4070 Å	2.54 \pm 0.46	1.50 \pm 0.29
[SVIII] 0.991 μm	1.87 \pm 0.19	1.11 \pm 0.14	[NeIII]+H1 3968 Å	6.27 \pm 0.63	3.71 \pm 0.46
[CaI] 0.985 μm	1.04 \pm 0.24	0.62 \pm 0.15	H8+HeI 3888 Å	3.60 \pm 0.61	2.13 \pm 0.39
[SiII] 0.953 μm	20.54 \pm 0.21	12.16 \pm 0.87	[NeIII] 3868 Å	20.41 \pm 1.63	12.08 \pm 1.29
[NII] 7378 Å	0.40 \pm 0.04	0.24 \pm 0.03	H9+HeII 3835 Å	1.09 \pm 0.51	0.65 \pm 0.31
[OI] 7320+7330 Å	1.87 \pm 0.11	1.11 \pm 0.10	[FeVII] 3758 Å	4.00 \pm 0.92	2.37 \pm 0.57
[ArIII] 7135 Å	3.20 \pm 0.22	1.89 \pm 0.19	[OII] 3727 Å	22.28 \pm 1.56	13.18 \pm 1.31
HeI 7065 Å	3.07 \pm 0.21	1.82 \pm 0.18	[NeV] 3426 Å	28.01 \pm 1.68	16.58 \pm 1.54
[ArVI] 7006 Å	1.60 \pm 0.11	0.95 \pm 0.09	[NeV] 3345 Å	10.0 \pm 0.80	5.92 \pm 0.63
[SiII] 6731 Å	5.34 \pm 0.32	3.16 \pm 0.29

Alonso-Herrero et al. (2003) while the temperature and amplitude of the blackbody function were left as free parameters. The result, displayed in the lower panel of Figure 2, show that the composite function, with a blackbody of temperature $T_{\text{bb}}=1200$ K, adequately describes the continuum distribution. Integrating the flux over these two components in the observed interval gives $F_{\text{bb}}=1.55 \times 10^{-11}$ erg cm $^{-2}$ s $^{-1}$ and $F_{\text{PL}}=5.60 \times 10^{-11}$ erg cm $^{-2}$ s $^{-1}$ for the blackbody and power-law functions, respectively. It means that in the NIR region, the former component accounts for 28% of the total continuum flux.

What is the origin of each of the two continuum components, both emitted in the inner 250 pc of the AGN? Given the composite nature of Mrk 766, harboring both a dusty active nucleus and a circumnuclear starburst, there are several possibilities. The power-law continuum can be associated to continuum emission from the AGN plus some contribution from circumnuclear stellar population and dust. Note that this power-law cannot simply be regarded as an extrapolation to the power-law used to describe the continuum in the UV and optical region. This is because in the optical, the continuum displayed by Mrk 766 is essentially flat, even in the UV region (see Figure 3 of GD96). This suggest that the continuum emission, at shorter wavelengths, is strongly reddened. Under the assumption that the power-law found in the NIR carries a significant contribution from the AGN, it can be used to find out an upper limit to the extinction affecting the UV and optical region. We determined that an at least a $E(B-V)=0.3$ to the continuum is necessary in order to a power-law of spectral index $\alpha=-0.44$ can adequately represents the AGN continuum in the optical region.

Regarding the nature of the excess of emission well described by a black body function, it could be related to a compact dust/molecular thick torus (Granato & Danese 1994) or result from emission from hot dust ($T>1000$ K). This reasoning follows similar distributions found in other AGN by Marco & Alloin (1998) and Marco & Alloin (2000).

3.2 The hot dust hypothesis

The excess of emission over the power-law distribution in the NIR region and its adequate representation obtained after adding a blackbody distribution suggest that it can be due to hot dust grains. The temperature derived from the fit ($T_{\text{bb}}=1200$ K) is near to the peak value for the hottest possible grains, i.e., graphite grains at their evaporation temperature, $T \sim 1500$ K, and higher than the sublimation temperature of silicate grains ($T \sim 1000$ K; Granato & Danese 1994). Considering that our spatial resolution is limited to ~ 250 pc, it is very likely that dust at higher temperatures exists closer to the central source, ruling out the possibility of silicates as the main component of the nuclear dust grains. This result does not exclude that silicate grains can exist within the NLR of Mrk 766. They still can be present within the observed region but a much lower temperature. Recalling that HST observations of Mrk 766 reveals filaments, wisps and irregular dust lanes around the unresolved nucleus (Malkan et al. 1998) and that the optical polarization of Mrk 766 is due to scattering from dust grains (Goodrich 1989), the dusty NLR scenario for Mrk 766 is strongly supported by the NIR data.

Using the temperature of the blackbody distribution derived above as the average temperature of the graphite grains and a K band flux of 1.03×10^{-25} erg s $^{-1}$ cm $^{-2}$ Hz $^{-1}$ at $2.2 \mu\text{m}$ found for the blackbody component after subtracting the power-law, we can roughly estimate the dust mass associated with the excess of emis-

sion. Following Barvainis (1987), the infrared spectral luminosity, in ergs s $^{-1}$ Hz $^{-1}$, of an individual graphite grain is:

$$L_{\nu, \text{ir}}^{\text{gr}} = 4\pi a^2 \pi Q_{\nu} B_{\nu}(T_{\text{gr}}) \quad (1)$$

where a is the grain radius, $Q_{\nu} = q_{\text{ir}} \nu^{\gamma}$ is the absorption efficiency of the grains and $B_{\nu}(T_{\text{gr}})$ is the Planck function for a grain of temperature T_{gr} . Adopting, as in Barvainis (1987), a value of $a=0.05 \mu\text{m}$ for graphite grains and $Q_{\nu}=0.058$ and setting $T_{\text{gr}}=1200$ K, we find $L_{\nu, \text{ir}}^{\text{gr}}=9.29 \times 10^{-18}$ ergs s $^{-1}$ Hz $^{-1}$.

The total number of emitting grains (hot dust) can be approximated as:

$$N_{\text{HD}} \approx \frac{L_{\text{NIR}}}{L_{\nu, \text{ir}}^{\text{gr}}} \quad (2)$$

Finally, for graphite grains, with density $\rho_{\text{g}}=2.26$ g cm $^{-3}$,

$$M_{\text{HD}} \approx \frac{4\pi}{3} a^3 N_{\text{HD}} \rho_{\text{g}} \quad (3)$$

Taking Mrk 766 at a distance of 51.6 Mpc ($z=0.0129$, $H_0=75$ km s $^{-1}$ /Mpc), we obtained $N_{\text{HD}}=3.54 \times 10^{45}$ and $M_{\text{HD}}=2.1 \times 10^{-3} M_{\odot}$.

The mass of hot dust derived for Mrk 766 is similar to that found in NGC 3783 ($2.5 \times 10^{-3} M_{\odot}$, Glass 1992) and NGC 1068 ($1.1 \times 10^{-3} M_{\odot}$, Marco & Alloin 2000); larger than that derived for NGC 1566 ($7 \times 10^{-4} M_{\odot}$, Baribaud et al. 1992) and NGC 4593 ($5 \times 10^{-4} M_{\odot}$, Santos-Lléo et al. 1995) and significantly smaller than that of NGC 7469 ($0.05 M_{\odot}$, Marco & Alloin 1998) and Fairall 9 ($0.09 M_{\odot}$, Clavel et al. 1989). Note that for all the above objects but Mrk 766, the mass of hot dust was derived from photometric observations. The spectral resolution of our data offers the possibility of examining a spectral feature not previously observed in such a detail.

Regarding to the location of the hot dust, our spectral resolution imply that it must reside within the inner 250 pc from the centre, since this is the region size covered by the nuclear NIR spectrum employed in this work (see § 2). The high temperature found for the dust, however, allows us to impose a tighter constraint to the location of the emitting region: it would be located in the central 100 pc. This value is deduced by inspecting Fig. 3 of Marco & Alloin (1998), where a plot of dust temperature as function of distance from the central source was constructed for NGC 7469. Note that in this reasoning, we have assumed that the dust in Mrk 766 has similar properties to that of NGC 7469. Further support to this value can be obtained following the results for NGC 1068 (Marco & Alloin 2000). These authors concluded that hot dust ($T_{\text{gr}}=1500$ K) should be extremely confined and located at a radius less than 4 pc. If that is also the case for Mrk 766, it is most likely that the excess of emission in the NIR is associated to the torus than to circumnuclear dust. Only high resolution spectroscopy will be able to disentangle this possibility. Whatever the case, our results provides the first direct spectroscopic evidence of hot dust in AGN and show the potential that NIR spectroscopy has at unveiling that component.

4 THE LINE EMITTING REGIONS

A careful inspection to the spectrum of Mrk 766 shown in Fig. 1 evidences prominent permitted emission lines of Fe II, H I, He I and O I and bright forbidden lines of [S III]. These features carry most of the energy radiated in the form of emission lines in the $0.8-1.3 \mu\text{m}$ interval. In addition, several coronal lines with

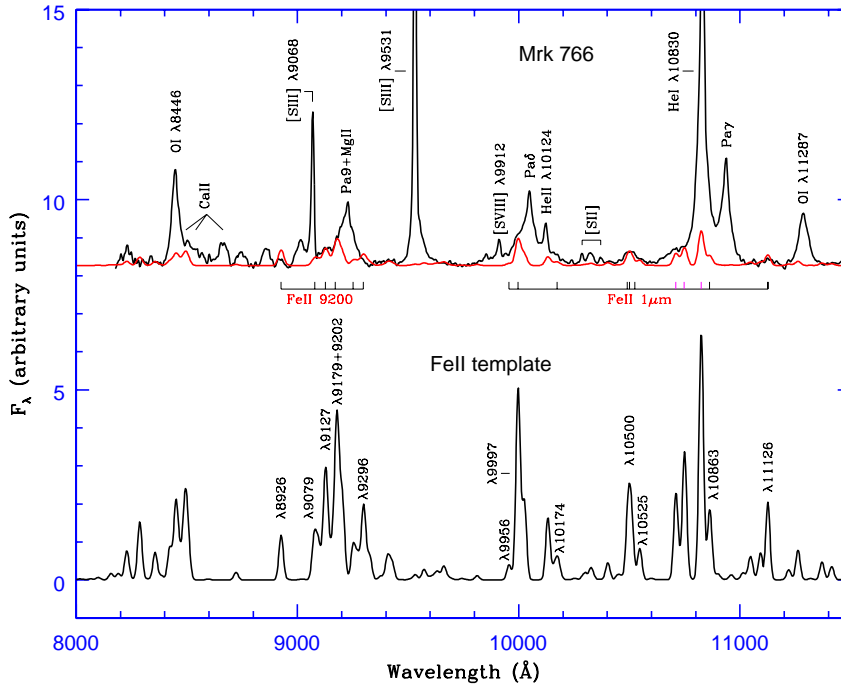


Figure 3. Top: Mrk 766 spectrum with the most important emission lines identified in the region between 0.8–1.1 μm . The continuum emission has been subtracted and the resultant spectrum displaced by an arbitrary amount for displaying purposes. The thick line is the best empirical Fe II template derived from the models of Sigut & Pradhan (2003). Note the good agreement between the template and most of Fe II features, mainly the 9200 \AA blend and the 1 μm lines. Bottom: Fe II Empirical template with the most important lines identified. Note that in order to ease the identification of individual lines, we show the template before being convolved with a Gaussian that matches the width of individual permitted lines of Mrk 766.

ionization potential (IP) of up to 350 eV, some of them previously observed in just a handful of AGN, are detected. Such is the case of [S VIII] 0.991 μm (IP=280.9 eV), [S IX] 1.252 μm (IP=328.3 eV), [Si VI] 1.963 μm (IP=166.7 eV), [Si IX] 3.936 μm (IP=303.17 eV), [Si X] 1.143 μm (IP=351.1 eV) and [Mg VIII] 3.03 μm (IP=224.95). Low ionization lines, with IP<13.6 eV, are also present (i.e., [C I], [Fe II] and [S II]).

The simultaneous observation of very high and neutral/low ionization lines imply that a wide variety of physical conditions must coexist within the central few hundred parsecs of this object. In the following sections, with the help of ionization models, we will extract information about the structure and physical state of the NLR, taking as reference, the observed continuum and emission line spectrum. A detailed analysis of the physical conditions and modeling of the BLR features will be discussed in a separate paper (Rodríguez-Ardila et al. 2004, in preparation). Here, we will briefly mention the most important features identified in the BLR spectrum of Mrk 766.

Few AGN with positive detection of NIR Fe II lines have been reported in the literature so far (Rudy et al. 2000, 2001; Nagar et al. 2002; Rodríguez-Ardila et al. 2002a). Here, we report the identi-

fication of the Fe II 9200 \AA blend and the Fe II 1 μm lines¹ in Mrk 766, as is shown in Fig. 3. In the upper part of the Figure, we have marked the strongest transitions identified. Overplotted, is the empirical template we derived. This work was done with the help of the NIR Fe II line list and models of Sigut & Pradhan (2003). A zoom of the empirical template, plotted at the bottom, was indeed constructed using the position and relative intensity of the lines listed by Sigut & Pradhan (2003). We then adjusted by eye most of the line intensities in disagreement with the model in order to get a better approximation to the observed spectrum.

The detection of NIR Fe II lines provides important information on the mechanism driving the formation of this ion. Primary cascade lines descending from the upper $5p$ levels to the lower e^4D and e^6D terms, thought to be pumped by Ly α fluorescence (Johansson & Jordan 1984; Sigut & Pradhan 1998, 2003), are located in the region between 8500 \AA and 9500 \AA . Their detection, as in Mrk 766, supports this mechanism as a competing one in the formation of the Fe II. Moreover, the 1 μm lines can also be pumped by Ly α fluorescence (see Figure 16 of Sigut & Pradhan 2003). The en-

¹ It is known under this name the set of Fe II lines located between 1 μm and 1.2 μm , among which 0.9997 μm , 1.0171 μm , 1.050 μm , 1.0863 μm and 1.1126 μm are the strongest ones

Table 3. FWHM, in km s^{-1} , of the detected lines in Mrk 766

Line	FWHM	Line	FWHM
[Ca vIII] 2.31 μm	≤ 360	He II (n) 1.16 μm	≤ 360
H ₂ 2.223 μm	≤ 360	He II (b) 1.16 μm	1220
Br γ (n)	≤ 360	[P II] 1.14 μm	≤ 360
Br γ (b)	1600	O I 1.128 μm	1270
H ₂ 2.212	≤ 360	Pa γ (n) 1.093 μm	≤ 360
He I (n) 2.058 μm	≤ 360	Pa γ (b) 1.093 μm	1720
He I (b) 2.058 μm	1890	He I 1.083 μm	780
H ₂ 2.033 μm	≤ 360	[S II] 1.037 μm	≤ 360
[Si VI] 1.96 μm	390	[S II] 1.033 μm	≤ 360
H ₂ 1.957 μm	≤ 360	[S II] 1.032 μm	≤ 360
[Fe II] 1.63 μm	≤ 360	[S II] 1.028 μm	≤ 360
[Si X] 1.43 μm	430	He II (n) 1.012 μm	≤ 360
Pa β (n) 1.281 μm	≤ 360	He II (b) 1.012 μm	1250
Pa β (b) 1.281 μm	1740	Pa δ (n) 1.004 μm	≤ 360
[Fe II] 1.257 μm	370	Pa δ (b) 1.004 μm	1700
[S IX] 1.252 μm	600	[S V III] 0.991 μm	≤ 360
[P II] 1.18 μm	≤ 360	[Ca I] 0.985 μm	≤ 360
...	...	[S III] 0.953 μm	≤ 360

ergy levels that are populated after their emission originate nearly 50% of the optical Fe II. This de-excitation channel has been overlooked for years and should be included in modeling the Fe II spectrum. Given the importance that the Fe II lines have in AGN studies, a paper describing the detection of NIR transitions and the physical information that can be derived for a sample of AGN, including Mrk 766, is currently in preparation.

In regard to the NLR, the width of the lines provide important clues about the velocity field of the emitting gas. This information will be useful for the models that are discussed in Secs. 5 and 6. Table 3 lists the FWHM measured for the lines detected in the spectrum.

The values of FWHM found in Mrk 766 indicate that all NLR lines but [S IX], [Si VI] and [Si X] are spectroscopically unresolved or in the limit of the spectral resolution. This agrees with the FWHM of the optical lines measured by GDP96. They found that H β , [O III], H α , [N II], [S II] and [S III] had widths of less than 250 km s^{-1} , well below our spectral resolution of 360 km s^{-1} . Véron-Cetty et al. (2001) also reported a FWHM of 330 km s^{-1} for [O III] $\lambda 5007$. This supports the existence of two distinct regions within the NLR of Mrk 766: one in which low and medium ionization lines are formed (the classical NLR), and another where the bulk of coronal lines (the so-called coronal line region, CLR) are emitted. Note, however, that no asymmetries are observed in the line profiles of the NIR coronal lines, consistent also with the observations of GDP96. This contrast to what is usually found in high-ionization lines in AGN (Penston et al. 1984; Erkens et al. 1997; Rodríguez-Ardila et al. 2004b). The lack of asymmetries suggest that the coronal lines are weakly related to outflowing material or strong shocks, as is usually claimed (Erkens et al. 1997). They should mostly originate from interaction between matter and radiation from the central source. This issue will be discussed in Sec. 6.

In addition to the permitted and forbidden lines, the NIR spectrum of Mrk 766 also displays conspicuous molecular H₂ lines, particularly in the K-band. Analysis of this emission is presented in Rodríguez-Ardila et al. (2004a), where it is concluded from the analysis of molecular line ratios and the vibrational and rotational temperature that thermal mechanisms drive the excitation of the H₂ gas. Moreover, X-rays from the central source can account for

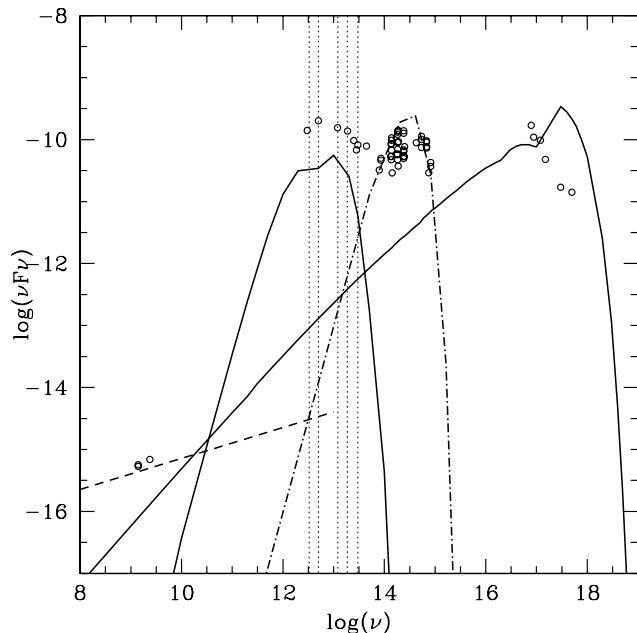


Figure 4. Comparison of the observed spectral energy distribution of Mrk 766 (open circles) and the model of Ark 564. The curves correspond to the fit to the Ark 564 continuum obtained by detailed modeling (Contini et al. 2003a). The dash-dotted line represents the old stellar population background. The vertical dotted lines refer to the IR wavelengths at 10, 16, 25, 60 and $100 \mu\text{m}$.

nearly 70% of the observed emission. The remaining 30% was attributed to the starbursts component, mostly via shock heating by supernova remnants. The molecular spectrum will not be further discussed through this text.

5 MODELING OF THE BROAD-BAND SPECTRAL ENERGY DISTRIBUTIONS

In order to model the SED of Mrk 766, some indication on which type of clouds may be present in the nuclear region is required. A comparative analysis of the observed continuum of Mrk 766 to that of other AGN provides a first approach to this problem.

The observed continuum spectra of Mrk 766 (open circles) is plotted in Fig. 4. As a guide, the energy distribution obtained in the modeling of Ark 546 (Paper I) is also plotted. The vertical dotted lines refer to wavelengths in the IR at 10, 16, 25, 60, and $100 \mu\text{m}$.

The data come from the NED². Observations in the optical-UV range (Gioia et al. 1990; Gavazzi & Boselli 1996; Gioia et al. 1990; De Vaucouleurs et al. 1991) have been corrected for internal reddening ($E(B-V)=0.5$). The other data refer to observations at lower frequencies (Balzano & Weedman 1981; Dressel & Condon 1978; Moshir et al. 1990; Becker et al. 1995; Maiolino et al. 1995; Rudy et al. 1982b; Spinoglio et al. 1995; Alonso-Herrero et al. 2003). Actually, Alonso-Herrero et al. claim that the nuclear fluxes at wavelengths greater than approximately $2 \mu\text{m}$ will not be significantly affected by moderate amounts of extinction. Moreover, the view of the torus through a fragmented screen of dust will dominate

² Nasa Extragalactic Database, <http://nedwww.ipac.caltech.edu>

the flux in the near-IR and simulate a low level extinction. No data appear in the UV where the correction could be significant.

The X-ray data, taken from Mason et al. (2003) using *XMM* observations, have been corrected for absorption using the coefficients given by (Zombeck 1990) adopting a column density $N_{\text{H}} = 10^{21} \text{ cm}^{-2}$.

In Fig. 4, the Mrk 766 SED is compared to the continuum spectrum obtained from the detailed modeling of Ark 564 (Paper I). Recall that the continuum which results from modeling represents reprocessed radiation (free-free and free-bound radiation) from clouds reached by the flux from the central source and heated by the shocks. The main reason for this comparison is the fact that, overall, both objects have similar spectral properties (Page et al. 1999). For example, they do not show evidence for the Big Blue Bump between the ultraviolet and the soft X-ray region. Moreover, they show a low ratio between the ultraviolet and the soft X-ray fluxes, implying a flat optical – X-ray energy distribution, as easily seen in Figure 4. In fact, for Mrk 766 and Ark 564, α_{ox} equals to -1.17 (this paper) and -1.08 (Romano et al. 2004), respectively, indeed flatter than the mean value of -1.63 for low-redshift radio-quiet objects (Yuan et al. 1998). It suggests that, in a first approach, the ionizing sources of Ark 564 and Mrk 766 are very similar.

Note, however, that the flux measurement in the X-rays region of Mrk 766 at the highest frequencies are lower than that for Ark 564. This may indicate that shock velocities as high as found in the NLR of the later ($V \geq 1000 \text{ km s}^{-1}$) are likely not to be present in the former. The data do not exclude a contribution to the X-rays coming from clouds with V_s of about 500 km s^{-1} . These type of clouds are found to be present in Seyfert 2 galaxies (Contini et al. 2004). Because the general behavior of the Mrk 766 continuum is different from those observed from Sy 2, we expect that if these intermediate velocity clouds are present in the NLR of Mrk 766, the fraction of the observed emission coming from these clouds should differ from the fraction in Seyfert 2.

Another important point is that the flux in the IR region is higher for Mrk 766 than for Ark 564, which could indicate that the dust-to-gas ratio, d/g , is higher. Notice that d/g depends on the ratio between the dust re-radiation flux intensity and the bremsstrahlung in the optical - NIR range (Contini et al. 2004). As discussed in the following sections, observations constraints that ratio, and the requirement for high d/g becomes less strong.

In summary, from the comparison of the SED of Mrk 766 and Ark 564, we conclude that both objects share a similar continuum energy distribution properties. It means that a safe starting point to model the line and continuum emission of the former is to assume a similar set of clouds successfully used in the modeling of the latter (Paper I)

6 MODELING THE LINE SPECTRA

By definition, the FWHM of the broad components of the permitted lines in NLS1s are $\leq 2000 \text{ km s}^{-1}$ (Osterbrock & Pogge 1985). Because the broad lines are narrower than those of classical Seyfert 1 galaxies, it is often difficult to unravel the narrow and broad components of permitted lines. This usually leads to an incorrect determination of the flux contribution of the hydrogen lines emitted by the NLR, which in turn could induce large errors when comparing the observed and calculated line ratios. In order to circumvent this problem, we chose to normalize the line intensities relative to that of [O III] $\lambda 5007+4959$ emission line flux as is shown in Table 2.

The criteria adopted to model Mrk 766 follow the same line of reasoning adopted for Ark 564 (Paper I) and is summarized as follows: (1) explain the emission-line spectrum and fit the continuum SED; (2) the velocities should be in agreement with the FWHM of the line profiles; (3) the ratio of calculated and observed lines relative to $\text{H}\beta$, $R(\text{H}\beta)_{\text{MC}}$, must be larger than unity, considering that the observed $\text{H}\beta$ flux contains also the contribution of the BLR.

A grid of models calculated for Ark 564 (Table 2 of Paper I) is rather complete, covering a large range of conditions suitable to describe the NLR of Seyfert galaxies. Moreover, recently, another specific grid of models was used to discuss the infrared continuum of Seyfert galaxies (Contini et al. 2004). All these results will be used as a starting point to explain the emission-line spectrum of Mrk 766.

In the previous section, we saw that the continuum SED of Mrk 766 and Ark 564 are similar. It means that a starting point in explaining the emission-line spectrum of Mrk 766 should be the use of a multi-cloud model similar to that adopted for Ark 564. However, as suggested by the FWHM of the observed line profiles in Mrk 766, the high V_s clouds found in Ark 564 (Paper I, models m13 and m14 with $V_s=1000 \text{ km s}^{-1}$ and $V_s=1500 \text{ km s}^{-1}$, respectively) are not expected to appreciably contribute to the observed spectrum. Thus, a first multi-cloud model is obtained for Mrk 766 adopting the same single-clouds used in the Ark 564 but with a different set of relative weights, which does not include models m13 and m14.

In addition, a recent analysis of the optical - infrared continuum spectra of AGN, Contini et al. (2004) showed that low V_s (100 km s^{-1}) - high density (1000 cm^{-3}) clouds are present in all types of Seyfert galaxies as well as clouds with intermediate velocity and density ($V_s = 500 \text{ km s}^{-1}$ and $n_0 = 300 \text{ s}^{-3}$). Since the observed continuum of Mrk 766 can not *a priori* exclude these type of clouds from the NLR modeling, a more consistent approach can be obtained by including them (models m15 and m16, Table 4). The relative weights of the single clouds were changed in order to obtain a better fit to the observed emission-line spectrum. The physical properties of the single-cloud models, their $\text{H}\beta$ absolute flux and the relative weights corresponding to the selected multi-cloud model (MC) are listed in the first rows of Table 4 (top). Table 4 also lists the contribution (in percent) of every single-cloud model to each emission-line. The (+) symbol near the line wavelengths indicates that the doublet intensities are summed up. We have removed from Table 4 the contributions smaller than 3% in order to have a clear view of the results. The comparison between the observed and modeled emission-line ratios is made in Table 5 and 6.

The multi-cloud model MC was calculated assuming that the radiation flux from the active centre is a power-law ($F \propto \nu^\alpha$) of intensity F_{h} at 1 Rydberg (in units of photons $\text{cm}^{-2} \text{ s}^{-1} \text{ eV}^{-1}$). The spectral indices $\alpha_{\text{UV}} = -1.5$ (between $13.6 \text{ eV} \leq E \leq 260 \text{ eV}$) and $\alpha_{\text{X}} = -0.4$ (for $E > 260 \text{ eV}$) were obtained from the best matching model since the spectrum of Mrk 766 is so rich in emission lines and continuum observations that it allows us to constrain the input continuum that produces them. This approach is preferred over the one that directly takes the observed far UV and X-ray data as input SED because the continuum that the NLR sees may differ from that emitted by active nucleus. In fact, other authors (e.g. Sako et al. 2003; Page et al. 2001; Vaughan & Fabian 2003; Constantin & Shields 2003) have found spectral indices steeper than those used here for the ionizing radiation. In order to test this hypothesis, we have calculated single-cloud models assuming an ionizing spectrum with a power law

Table 4. Percent contribution of each model to the multi-cloud model MC

	m1	m2	m3	m4	m6	m7	m8	m9	m10	m11	m12	m15	m16
V_s^1	100	100	100	100	150	150	300	500	500	500	500	500	100
n_0^2	100	100	100	100	100	600	100	100	100	700	700	300	1000
F_h^3	1.(9)	1.(10)	1.(11)	7.(11)	1.(12)	3.(12)	-	-	5.(12)	-	1.(11)	1.(11)	-
D^4	1.	3.	3.	3.	0.01	0.003	3.	3.	3.	3.	1.	1.	1.
$H\beta^6$	0.014	0.1	0.46	0.61	7.4(-3)	0.37	1.8(-4)	1.9(-3)	24.9	0.015	8.7(3)	678.7	0.66
d/g^5	10.	10.	1.	1.	1.	1.	10.	1.	10.	5.	1.	10.	0.03
wr	5.5(-3)	5.5(-3)	2.8(-3)	2.8(-3)	8.3(-3)	5.5(-3)	0.83	0.083	1.4(-4)	0.028	2.5(-6)	1.4(-5)	0.028
[Nev] 3425	-	-	-	19.	-	50.	3.1	-	23.	-	-	-	-
[OII] 3727+	-	9.3	11.	-	-	-	46.	5.2	-	3.8	-	3.4	16.
[FeVII] 3758	-	-	-	33.	-	8.5	10.	-	41.	5.1	-	-	-
[NeIII] 3869+	-	-	9.4	14.	-	-	7.7	-	67.	-	-	-	-
[SII] 4070	-	9.2	41.	-	-	-	4.9	-	-	17.	18.	4.6	-
[OIII] 4363	-	-	8.2	50.	-	-	8.9	-	21.	5.0	-	-	-
HeII 4686	-	-	3.5	12.	-	24.	-	-	43.	-	6.5	7.4	-
[ArIV] 4740	-	-	-	49.	-	-	-	-	44.	-	-	-	-
[OIII] 5007+	-	-	19.	36.	-	-	-	-	17.	-	13.	7.2	-
HeI 5876	-	-	-	-	-	-	-	-	-	-	6.1	-	90.
[FeVII] 6086	-	-	-	32.	-	9.2	6.6	-	47.	3.4	-	-	-
[OI] 6300	4.5	27.	37.	-	-	-	-	5.	-	23.	-	-	-
[FeX] 6375	-	-	-	20.	-	40.	4.4	3.1	23.	9.1	-	-	-
[NII] 6548+	4.0	24.	23.	-	-	-	8.3	3.8	-	7.6	18.	11.	-
[SII] 6717	3.7	25.	57.	-	-	-	3.9	3.5	-	4.	-	-	-
[SII] 6731	3.	21.	54.	-	-	-	4.4	4.3	-	7.3	-	-	-
[ArIII] 7135	-	-	16.	-	-	-	-	-	-	-	54.	23.	-
[OII] 7320+	-	-	-	-	-	-	37.	3.6	-	22.	3.	-	28.
[SIII] 0.95	-	3.9	14.	-	-	-	-	-	-	-	51.	26.	-
[SVIII] 0.99	-	-	-	20.	-	51.	-	-	22.	-	-	-	-
[SII] 1.028	-	9.0	39.	-	-	-	4.9	-	-	17.	18.	4.6	-
HeI 1.08	-	-	-	-	-	-	-	-	-	-	19.	6.2	71.
[SIX] 1.25	-	-	-	22.	-	38.	3.9	-	24.	7.1	-	-	-
[SIX] 1.43	-	-	-	20.	6.6	38.	-	-	26.	6.	-	-	-
[SIV] 1.96	-	-	-	29.	-	11.	-	-	52.	-	-	-	-
HeI 2.06	16.	39.	10.	-	-	-	-	-	-	-	-	33.	-
[MgVIII] 3.03	-	-	-	75.	4.4	-	11.	-	-	7.2	-	-	-
[SIX] 3.93	-	-	-	68.	9.9	-	6.5	3.7	-	12.	-	-	-

¹ in km s^{-1} ; ² in cm^{-3} ; ³ in photons $\text{cm}^{-2} \text{s}^{-1} \text{eV}^{-1}$ at 1 Ryd; ⁴ in 10^{19}cm ; ⁵ in 10^{-15} ; ⁶ in $\text{erg cm}^{-2} \text{s}^{-1}$

index $\alpha_{UV}=-2.4$ and $\alpha_X = -1.7$, which correspond to the indices reported by Constantin & Shields (2003). These new models were obtained with the same V_s and n_0 as shown in Table 7 and were used to built the multi-cloud model labeled MCS.

Although a reasonable fit to the data can be obtained with the cloud models listed in Table 7, we found that a high fraction of the line fluxes, corresponding to both high and low -ionization lines, are originated from high velocity clouds ($V_s=1000 \text{ km s}^{-1}$, model m13 of Paper I). Such type of clouds are excluded because the measured FWHM of the line profiles in the nuclear spectrum of Mrk 766 rules out the existence of gas motion with velocities above 500 km s^{-1} within the NLR. We therefore adopt model MC discussed above to obtain the SED of the continuum and to compare its prediction to the observations. Notice that the observed soft X-ray index is -1.77 , while for the modeling we adopt -0.4 . The discrepancy between both indices suggests that the NLR clouds see a harder, different continuum, than that we detect. This same conclusion had previously been reached by several authors (Binette et al. 1989, 1993; Korista et al. 1997) in studying the physical conditions of the BLR using photoionization models. Moreover, in our models, the observed soft X-ray continuum is due to bremsstrahlung

originating in the clouds that re-process the central ionizing radiation.

Before concluding this section, it is important to comment on the values listed in Table 5, where the ratio between the calculated and observed line ratios relative to [O III], $R([\text{O III}]_{\text{MC}})$, and to $H\beta$, $R(H\beta)_{\text{MC}}$, are listed.

The calculated emission-line ratios for most lines except [Mg VIII] and [S IX] are, within the error bars, good by a factor of 2. The latter two lines are underestimated by a larger factor.

It is found that a large contribution to the bulk of the line fluxes comes from radiation-dominated clouds. This is the case, for example, of the NIR coronal lines. In them, the radiation flux from the active centre strongly contributes to the ionization of gas, which is heated to high temperatures ($T_e > 1.5 \cdot 10^5 \text{ K}$) by the shock. Note that even in radiation-dominated clouds the shock is also accounted for. On clouds propagating outwards from the AC, it acts on the edge opposed to that facing the radiation flux. The coupled effect of the shock and the radiation flux determine the distribution of the temperature throughout the cloud. The temperature in the postshock region, immediately after the shock front is $T_e = 1.5 \times 10^5 (V_s/100)^2 \text{ K}$ decreasing downstream due to energy

Table 5. Comparison of observational data with model results. The indices MC and MCS identify the solution obtained with the two different continua used in the modeling. For model MC, the input continuum is the one from the best matching model ($\alpha_{UV} = -1.5$ and $\alpha_X = -0.4$). For MCS, the input continuum is the one derived by Constantin & Shields (2003). See text for further details.

	$(I_\lambda/I_{[OIII]})_{obs}$	$(I_\lambda/I_{[OIII]})_{MC}$	$R([OIII])_{MC}$	$R(H\beta)_{MC}$	$R([OIII])_{MCS}$	$R(H\beta)_{MCS}$
[NeV] 3425+	22.5	20.6	0.91	1.23	1.64	4.8
[OII] 3727+	13.18	7.74	0.59	0.79	1.96	5.7
[FeVII] 3758	2.37	2.99	1.27	1.7	2.5	7.4
[NeIII] 3869+	15.8	13.7	0.87	1.17	0.5	1.44
[SII] 4070+	1.5	1.3	0.86	1.16	0.85	2.5
[OIII] 4363	2.05	1.81	0.9	1.2	0.84	2.5
HeII 4686	4.34	5.2	1.2	1.6	3.08	9.12
[ArIV] 4740+	0.74	2.1	2.9	3.9	2.4	2.4
[OIII] 5007+	100.	100.	1.	1.34	1.	3.
HeI 5876	8.14	37.2	4.6	6.14	0.3	0.9
[FeVII] 6086	1.42	3.43	2.4	3.25	5.4	16.
[OI] 6300+	2.4	2.37	0.99	1.33	1.28	3.8
[FeX] 6375	0.27	1.65	6.1	8.26	4.7	14.
[NII] 6548+	13.0	6.6	0.51	0.68	0.6	1.65
[SII] 6717	2.45	4.7	1.9	2.6	0.68	2.01
[SII] 6731	3.15	4.9	1.57	2.1	0.7	2.1
[ArIII] 7135	1.89	1.9	1.0	1.35	0.59	1.75
[OII] 7320+	1.11	1.1	1.05	1.41	2.9	2.02
[SIII] 0.95+	12.16	10.	0.82	1.1	0.5	1.5
[SvIII] 0.99	1.1	0.98	0.89	1.12	0.7	2.02
[SII] 1.28	1.04	0.9	0.85	1.13	1.07	3.2
HeI 1.08	21.2	39.5	1.86	2.5	0.18	0.53
[SiX] 1.25	0.79	0.26	0.33	0.45	0.22	0.66
[SiX] 1.43	0.53	0.57	1.07	1.44	0.52	1.53
[SiVI] 1.96	1.1	1.6	1.5	2.0	3.5	10.5
HeI 2.06	0.57	0.13	0.23	0.31	0.62	1.83
[MgVIII] 3.027	1.74	0.61	0.35	0.48	0.63	1.85
[SiX] 3.93	1.10	1.77	1.6	2.15	2.1	6.3

Table 6. Observed and predicted UV emission lines for the model MC.

Line	F_{obs}^1	$F_{obs}/H\beta$	$(I_\lambda/H\beta)_{obs}^2$	$(I_\lambda/H\beta)_{MC}$	$R(H\beta)_{MC}$
Ly α 1214	29.78 \pm 0.32	0.19	5.46	29.	5.4
N v 1240	2.10 \pm 0.17	0.013	0.31	1.0	3.23
C II 1335	1.15 \pm 0.19	0.007	0.10	-	-
Si IV+O IV] 1400	4.31 \pm 1.25	0.027	0.30	0.75	2.5
N IV] 1486	1.81 \pm 0.82	0.012	0.11	0.42	3.8
C IV 1549	17.63 \pm 0.94	0.112	0.88	6.1	6.9
He II 1640	5.13 \pm 0.52	0.033	0.24	1.1	4.5
Si III] 1892	2.05 \pm 0.87	0.013	0.11	0.13	1.17
C III] 1908	11.75 \pm 1.38	0.075	0.66	0.38	0.57
C II] 2327	4.07 \pm 1.68	0.026	0.23	-	-
[Ne IV] 2423	4.45 \pm 0.70	0.028	0.17	0.15	0.9
Mg II 2797	26.26 \pm 1.41	0.17	0.51	0.24	0.47
H β	157.3 \pm 5.60	1.	1.	1.	1.

¹ in 10^{-15} erg cm $^{-2}$ s $^{-1}$; ² corrected for E(B-V)=0.5

losses by free-free, free-bound, line emission, and collision heating of dust. The stratification of the ions downstream follows the distribution of the temperature described in Contini & Viegas (1991). Our results suggest that the coronal lines in Mrk 766 are formed mainly from the interaction of matter and radiation from the central source rather than shocks. A similar result is found from the analysis of optical and NIR coronal lines in a sample of Seyfert 1 and 2 galaxies by Rodríguez-Ardila et al. (2004, in preparation).

They report, using high-spatial resolution spectroscopy, extended coronal emission within the few tens of parsecs from the active nucleus and points out that radiation from the central source are, in fact, able to power them. Support for this scenario is also provided by (Prieto et al. 2004) by means of VLT NIR observations of Circinus. Other evidence, however, supports the hypothesis that coronal lines are most likely associated to outflowing winds (Erkens et al. 1997; Rodríguez-Ardila et al. 2002b).

Table 7. Percentage contribution of the individual clouds to the multi-cloud model MCS, calculated with steep spectral indices.

	m6	m7	m8	m9	m10	m13
V_s^a	150	150	300	500	500	1000
n_0^b	100	600	100	100	100	1000
F_h^c	1(12)	3(12)	-	1(10)	5(12)	5(12)
D^d	.01	.003	3.	3.	3.	.1
$H\beta$ (MCS) ^e	7.(-3)	0.65	1.9(-4)	5.72	62.4	3.5
wr(MCS)	0.21	8(-4)	0.79	1(-5)	2(-5)	1.3(-4)
[NeV]3425	84.	-	11.	-	-	-
[OII]3727	-	81.	17.	-	-	-
[FeVII]3758	63.	-	32.	-	-	-
[NeIII]3869+	4.	30.	27.	-	28.	4.7
[SII]4070	-	-	21.	-	-	73.
[OIII]4363	-	26.	59.	-	7.5	-
HeII 4686	50.	12.	-	-	36.	-
[ArIV]4740	-	70.	15.	-	14.	-
[OIII]5007+	5.9	43.	14.	-	37.	-
HeI 5876	4.4	4.5	8.3	-	9.7	75.
[FeVII]6086	75.	4.4	19.	-	-	-
[OI]6300	-	-	15.	23.	-	62.
[FeX]6375	10.	-	36.	-	-	53.
[NII]6548+	-	-	43.	33.	-	23.
[SII]6717	-	-	74.	4.	8.4	12.
[SII]6731	-	-	63.	4.5	11.	20.
[ArIII]7135	-	9.5	-	31.	58.	-
[OII]7320+	-	-	77.	8.7	-	14.
[SIII]0.95	-	-	17.	28.	51.	-
[SVIII]0.99	64.	-	23.	-	-	13.
[SII].028	-	-	22.	-	-	73.
HeI 1.08	-	22.	8.9	-	18.	47.
[SIX]1.25	6.4	-	35.	-	-	58.
[SiX]1.43	-	-	24.	-	-	75.
[SiVI]1.96	81.	9.1	6.4	-	-	-
HeI 2.06	-	-	-	98.	-	-
[MgVIII]3.03	54.	-	40.	-	-	5.7
[SiIX]3.93	17.	-	31.	-	-	52.

^a in km s^{-1} ; ^b in cm^{-3} ; ^c in $\text{photons cm}^{-2} \text{s}^{-1} \text{eV}^{-1}$ at 1 Ryd; ^d in 10^{19} cm ; ^e in $\text{erg cm}^{-2} \text{s}^{-1}$.

It is also possible to have a strong contribution from shock-dominated clouds, as is, for example, the ratio $[\text{O II}]3727+ / [\text{O III}]5007+$. The high value of the ratio comes from the fact that 70% of the $[\text{O II}] 3727+$ line flux comes from that type of clouds (models m8, m9, m11, and m16).

The optical $[\text{N II}]$ lines are underestimated by the multi-cloud model MC by about a factor of 2. Since both $R([\text{O III}])_{MC}$ and $R(H\beta)_{MC}$ are less than unity, we conclude that the N/H abundance is about a factor of 2 higher than solar.

On the other hand, all Fe lines are overestimated, indicating that Fe is depleted, probably trapped into small grains. Also, $[\text{Ar IV}] 4740+$ are overestimated, perhaps due to a too high Ar/H relative abundance. We notice that in order to improve the results for the Fe lines, both model MC and MCS require that Fe/H be depleted by a factor of ~ 3 . Furthermore, ratios of calculated to observed line ratios (relative to $H\beta$), indicate an average contribution of the broad line region to the observed $H\beta$ of about 40% (see columns 5 and 7 of Table 5). In Ark 564, that contribution was found to be lower ($\sim 30\%$).

It is important to note that photoionization models for the NLR and the extended emission region of Mrk 766 were also presented by GP96. They used two types of ionizing continua: a

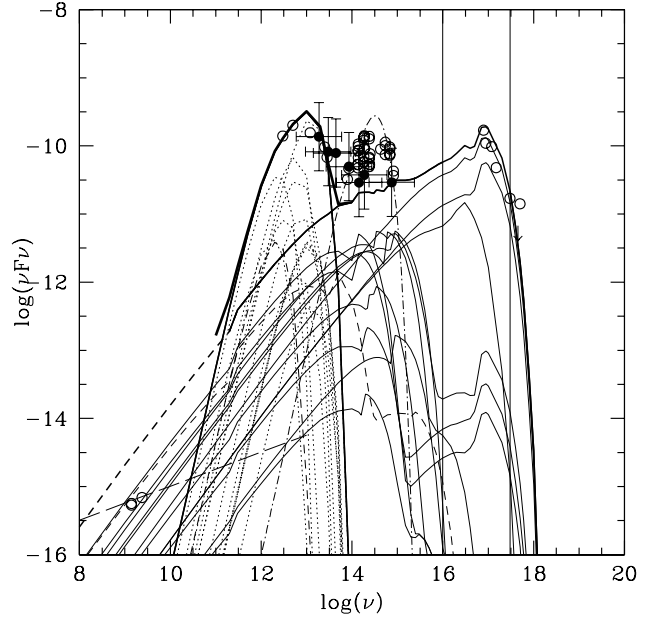


Figure 5. The observed and calculated continuum of Mrk 766. The data come from NED (open circles) and Alonso-Herrero et al. (2003) (solid circles). The thin lines correspond to the results from the single clouds contributing to the best multi-cloud model MC, with dotted lines representing dust emission and solid lines bremsstrahlung emission from those clouds. The two vertical solid lines define the frequency range in which the X-ray radiation is absorbed. The spectrum obtained with the low velocity, high density single-cloud model m16 is shown by the thin dashed line. The very thick solid line shows the continuum corresponding to the multi-cloud model MC.

power-law, with spectral indices -1 and -1.5 or a blackbody with effective temperatures $T_{\text{eff}}=10^5 \text{ K}$ and $2.2 \times 10^5 \text{ K}$. The comparison between the calculated and observed emission line ratios of $[\text{O III}]/H\beta$, $[\text{O II}]/H\beta$, $[\text{O I}]/H\alpha$, $[\text{N II}]/H\alpha$, $[\text{S II}]/H\alpha$ and $[\text{S III}]/H\alpha$ showed that both the power-law and blackbody could explain the observed data. Clearly, the inclusion of emission lines located in other wavelengths intervals (NIR and UV), as was done here, gives more consistency to the modeling and allows a better understanding of the physical conditions in the NLR of Mrk 766.

Finally, the observed and calculated UV lines relative to $H\beta$ are compared in Table 6. The results show that there is a high contribution of model MC, i.e., of the NLR, to the UV lines, particularly for N V , $\text{N IV}] \text{C IV}$ and He II .

7 THE CONTINUUM SED OF MRK766

In order to consistently model the line and continuum spectra, it is necessary to cross check one another until a fine tune for both is found. Therefore, the results presented in the previous section were selected after this checking was performed.

The calculated SED of Mrk 766 obtained from model MC is compared to the observations in Fig. 5, where the data taken from NED (open circles) and from Alonso-Herrero et al. (2003) (solid circles) are plotted. Notice that the errors for the Alonso-Herrero et al.'s data are about 30%. The thin dotted lines and the thin solid lines represent the emission from the single clouds due to dust and bremsstrahlung, respectively. The thin dashed lines correspond to the results from model m16 (see Contini et al. 2004, Sect. 3), which

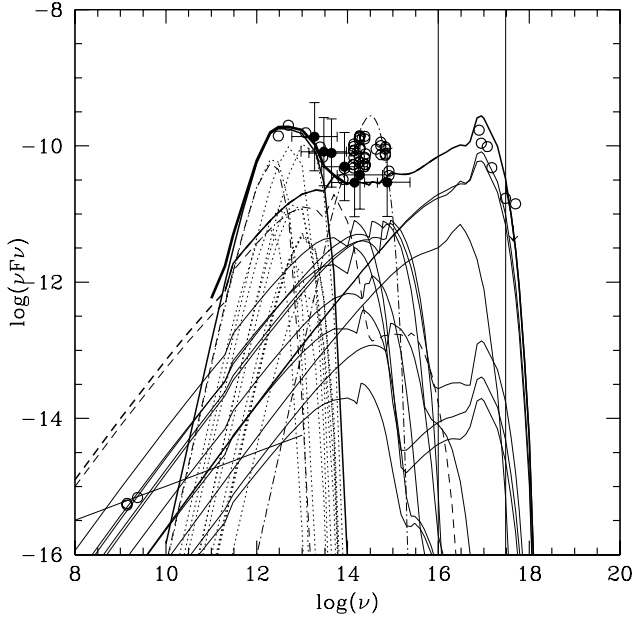


Figure 6. The observed and calculated continuum of Mrk 766. The multi-cloud model was derived assuming a relative weight for the low velocity, high density single-cloud (model m16) a factor 10 higher than for MC (see text). Same notation as in Figure 5.

is included in the multi-cloud model MC with other single-cloud models used to explain the Ark 564 spectra. The thick solid line represents the multi-cloud model with separated curves representing re-radiation by dust and bremsstrahlung, while the very thick line represents the sum of these two curves. Finally, the dash-dotted line corresponds to the background old star population.

Another SED, obtained by adopting a relative weight for model m16 higher by a factor of 10 than the value used in model MC, is also shown in Fig 6. However, regarding the corresponding emission-line spectrum, this alternative multi-cloud model leads to very low line intensities relative to $H\beta$ ($R(H\beta)_{MC}$) and was dropped.

The data in the radio range (long-dashed line) show that radiation at these frequencies is due to synchrotron created by the Fermi mechanism at the shock front. At long wavelengths, bremsstrahlung emission is self-absorbed, particularly for models with a high density downstream, which depends on n_0 , B_0 , and V_s . Actually, the optical thickness becomes larger than unity for $T \leq 10^4$ K, $\nu \leq 10^{11}$ Hz, for a slab of at least 1.3 pc downstream of high density clouds (e.g. model m12) because compression leads to densities higher than 2×10^9 cm^{-3} (Osterbrock 1988). Thus, the contribution to bremsstrahlung in the radio range of relatively high density clouds must be negligible.

Overall, the observed and calculated SED are in very good agreement, as can be seen in Figure 5. This confirms and strengthens the validity of our approach. The largest discrepancy is located in the X-ray region, where the model overpredicts the observed emission. Here, the rapid and strong variability of the X-rays radiation, of up to a factor of 2 on a time scale of a few thousand seconds (Mason et al. 2003), clearly indicates that the bulk of this radiation is directly emitted by the central source and the BLR. However, it is expected that a small fraction of the X-ray emission arises from high velocity clouds. Indeed, the bremsstrahlung

calculated by models m11 and m12 overpredict the data. Notice however that a possible absorption of the X-rays by these kinds of clouds is not taken into account. In fact, absorption must occur firstly because of the large geometrical thickness of the clouds ($D=10$ pc) with $V_s=500$ km s^{-1} and $n_0=700$ cm^{-3} , and secondly, because of the high densities downstream due to compression ($n/n_0 \leq 10$, depending on V_s , n_0 , and B_0). Under these conditions, column densities higher than 10^{23} cm^{-2} occur in the clouds producing a strong absorption of the high energy radiation from 13.6 eV up to 500 eV (Zombeck 1990). Clouds with lower values of D , V_s and n_0 unlikely absorb X-rays.

8 DISCUSSION AND CONCLUDING REMARKS

As part of a wide program to understand the mechanisms at work in the NLR of NLS1 galaxies, we have carried out a detailed study of the galaxy Mrk 766. For this purpose, the first spectroscopic observations covering simultaneously the interval $0.8\text{--}4$ μm is presented along with the measurement of the most conspicuous emission line fluxes detected in that region. These lines are used as additional constraints in order to unveil the physical conditions of the NLR gas. The single-cloud models adopted for modeling are those previously used for the analysis of the continuum and emission-line spectra of Ark 564. However, the two high velocity cloud models used for the later object were removed from the multi-cloud model that fits Mrk 766 because the X-rays flux is lower when compared to the continuum emission in other frequency ranges and the FWHM of the emission lines indicate lower velocities. On the other hand, two cloud models suggested by the fit of the NIR data of Alonso-Herrero et al. (2003) sample were added. Indeed, after including these single-cloud models, a better fit of the line intensities relative to $[O\text{III}]$ and $H\beta$, as well as of the continuum, were obtained.

As already found in the analysis of other individual AGN, shock dominated models have higher relative weights because the absolute $H\beta$ flux is lower. The shock velocities range between 100 km s^{-1} and 500 km s^{-1} , the preshock densities between 100 cm^{-3} and 1000 cm^{-3} and the radiation fluxes from the active center from 10^9 to $5 \cdot 10^{12}$ photons cm^{-2} s^{-1} eV^{-1} at 1 Ryd with spectral indices of $\alpha_{UV}=-1.5$ and $\alpha_X=-0.4$. Higher power-law indices were dropped because they did not lead to satisfactory explanation of the observed spectra.

The d/g ratios are between 10^{-15} and 10^{-14} by number (4×10^{-5} to 4×10^{-4} by mass for silicates) and reach the lowest value in clouds corresponding to model m16 with $d/g = 3 \cdot 10^{-17}$ ($\geq 10^{-6}$ by mass).

We consider that $R=A_V/E(B-V) \sim 3.1$ (Cardelli et al. 1989) and $A_\lambda=1.086 \tau_\lambda$ with $\tau_\lambda=Q_\lambda \pi a_{gr}^2 N_{gr}$, where Q_λ is the extinction efficiency, a_{gr} the grain radius, and N_{gr} is the column density of dust. $N_{gr} = n \times d/g \times x$, where n is the gas density downstream which increases with n_0 and V_s , and x is the geometrical thickness of the dust slab. Adopting $E(B-V)=0.5$, $Q \sim 2$, $n=10^4\text{--}10^5$ cm^{-3} , $d/g = 10^{-15} - 10^{-14}$, $x \sim 0.2 - 20$ pc in good agreement with the geometrical thickness of the clouds given in Table 2.

The important contribution to the NIR SED of Seyfert galaxies of high density-low velocity clouds, corresponding to model m16, was demonstrated by Contini et al. (2004), who also raised questions about their location in the galaxies and their dust-to-gas ratios. With the data already discussed, we are now able to roughly estimate the distance from the active center. To this purpose, we use the $[O\text{II}]$ 7320+ line, which is nicely fitted by the multi-cloud

model and shows the highest percentage contribution from model m16 relative to the other forbidden lines. This type of cloud is also responsible for emission of the permitted lines He I 5876 Å and He I 1.083 μm. However, since the latter two lines include the contribution from the BLR, any location of the clouds deduced from these lines may be mistaken. From Table 4, we see that the larger contribution to the [O II] 7320+ emission-line comes from the single-clouds m8, m10 and m16. Thus, assuming that the single-clouds are co-spatial, their distance r from the central source can be estimated from the expression,

$$F_{[OIII]_{obs}} \times d^2 = (\sum_i wr(i) \times H\beta(i) \times ([OII]/H\beta)_{calc}(i)) \times r^2 (4)$$

where $i=1,2,3$, refers to the three types of single clouds, d is the distance to Mrk 766, $wr(i)$ and $H\beta(i)$ are given in Table 4, and the line intensity, relative to $H\beta$, is equal to 4.64, 1.5, and 0.04, respectively, for m8, m11 e m16. Assuming $H_0=75 \text{ km s}^{-1}/\text{Mpc}$, the distance of Mrk 766 from Earth is $d=51.6 \text{ Mpc}$. Thus, we obtain an average distance of $r=160 \text{ pc}$. Since usually higher velocity clouds (m8 and m11) are closer to the center, r is probably a lower limit to the distance of the low-velocity clouds (m16). The average distance obtained for the clouds is also in very good agreement to the region size of 250 pc covered by the nuclear NIR spectrum employed in this work. This gives further consistency to our modeling an approach to describe the physical conditions of the NLR of Mrk 766.

The high n_0 and the low dust-to-gas ratio of the clouds m16 may indicate that they are the residual of matter which was already compressed by a previous blast wave propagating outwards. The velocity of the blast wave was high enough to destroy most of the dust grains by sputtering, i.e., $V_s \geq 200 \text{ km s}^{-1}$ (Contini et al. 2004). Besides compression, another effect of the blast wave is fragmentation, which follows in the turbulent regime created by shocks. Indeed, in this model, because of the relative high density, the postshock cooling rate is high and the gas recombines at a distance $\leq 10^{17} \text{ cm}$ from the shock front. Beyond this distance the gas temperature drops to $< 500 \text{ K}$. Thus, the clouds are radiation-bound and the geometrical thickness (D) adopted for model m16 can be regarded as an upper limit. Note that the clouds corresponding to model m16 could be geometrically thin, strengthening the hypothesis of fragmentation.

In view of the important role of NLS1 in the determination of metallicities in AGN, in particular through the nitrogen lines (e.g. Shemmer & Netzer 2002), the results of the multi-cloud model suggest that a N/H higher than solar by a factor ≥ 2 would be in agreement with the $[N II]+/[O III]+$ line ratio (Table 5). We also suggest that iron is depleted from the gaseous phase because of its emission line ratios are systematically overpredicted.

Finally, let us conclude that the coupled effects of photoionization and shocks allowed us to explain most of the features observed in both the line and continuum spectra of the NLS1 Mrk 766.

ACKNOWLEDGMENTS

We are grateful to the referee, Dr. D. Grupe, for many valuable comments to improve this manuscript. This paper is partially supported by the Brazilian funding agencies FAPESP (00/06695-0) and CNPq(304077/77-1 and 309054/03-6) to ARA and SMV. This research has made use of the NASA/IPAC Extragalactic Database (NED) which is operated by the Jet Propulsion Laboratory, California Institute of Technology, under contract with the National Aeronautics and Space Administration.

REFERENCES

- Alonso-Herrero, A., Quillen, A.C., Rieke, G.H., Ivanov, V.D., Estathiou, A. 2003 astro-ph/0303617
- Alonso-Herrero, A., Simpson, C., Ward, M. J., Wilson, A. S. 1998, ApJ, 495, 196
- Balzano, V.A., Weedman, D.V. 1981 ApJ, 243, 756
- Baribaud, T., Alloin, D., Glass, I., Pelat, D. 1992, A&A, 256, 375
- Barvainis, R. 1987, ApJ, 320, 537
- Becker, R.H., White, R.L., Helfand, D.J. 1995 ApJ, 450, 559
- Binette, L., Prieto, A., Szuszwicz, E., Zheng, W. 1989, ApJ, 343, 135
- Binette, L., Fosbury, R. A., Parker, D. 1993, PASP, 105, 1150
- Boller, T., Brandt, W. N., Fink, H. 1996, A&A, 305, 53
- Boroson, T. A. 2002, ApJ, 565, 78
- Cardelli, J.A., Clayton, G.C., Mathis, J.S. 1989, ApJ, 345, 245
- Clavel, J., Wamsteker, W., Glass, I. S. 1989, ApJ, 337, 236
- Constantin, A., Shields, J.C. 2003, PASP, 115, 592
- Contini, M., Viegas, S.M. 2001, ApJS, 132, 211
- Contini, M., Rodríguez-Ardila, A., Viegas, S.M. 2003a, A&A, 408, 101, Paper I
- Contini, M. Viegas, S.M., Prieto, M.A. 2004, MNRAS, 348, 1065
- Contini, M. Viegas, S.M. 1991, A&A, 251, 27
- De Vaucouleurs, G., De Vaucouleurs, A., Coewin Jr. H.G., Buta, R.J., Paturel, G., Fouque, P. 1991, Third Reference Catalog of Bright Galaxies, Version 3.9
- Cushing, M. C., Vacca, W. D., Rayner, J. T. 2004, PASP, 116, 362
- Dressel, L.L., Condon, J.J. 1978 ApJS, 36, 53
- Edelson, R. A., Malkan, M. A. 1986, ApJ, 308, 59
- Erkens, U., Appenzeller, I., Wagner, S. 1997, A&A, 323, 707
- Gaskell, C. M., Goosmann, R. W., Antonucci, R. R., Whysong, D. H. 2004, ApJ, *in press* (astro-ph/0309595).
- Gavazzi, G., Boselli, A. 1996 ApL&C, 35, 1
- Gioia, I.M., Maccacaro, T., Schild, R.E., Wolter, A., Stocke, J.J., Morris, S.L., Henry, J.P. 1990 ApJS, 72, 567
- Glass, I. 1992, MNRAS, 256, 23P
- Goodrich, R. W. 1989, ApJ, 342, 224
- González Delgado, R.M., Pérez, E. 1996 MNRAS, 278, 737
- Granato, G. L., Danese, L. 1994, MNRAS, 268, 235
- Grupe, D. 2004, AJ, 127, 1799
- Grupe, D., Thomas, H.-C. 2002, A&A, 386, 854
- Grupe, D., Thomas, H.-C., Beuermann, K. 2001, A&A, 367, 470
- Grupe, D., Wills, B. J., Wills, D., Beuermann, K. 1998, A&A, 333, 827
- Johansson, S., Jordan, C. 1984, MNRAS, 210, 239
- Knop, R. A., Armus, L., Matthews, K., Murphy, T. W., Soifer, B. T. 2001, ApJ, 122
- Korista, K., Ferland, G., Baldwin, J. 1997, ApJ, 487, 555
- Kukula, M.J., Pedlar, A., Baum, S.A., O'Dea, P. 1995, MNRAS, 276, 1262
- Leighly, K. M. 1999a, ApJS, 125, 297
- Leighly, K. M. 1999b, ApJS, 125, 317
- Leighly, K. M. 1996, ApJ, 469, 147
- Lutz, D., Sturm, E., Genzel, R., Spoon, H. W. W., Moorwood, A. F. M., Netzer, H., Sternberg, A. 2003, A&A, 409, 867
- MacKenty, J. W. 1990, ApJS, 72, 231
- Maiolino, R., Ruz, M., Rieke, G.H., Keller, L.D. 1995 ApJ, 446, 561
- Malkan, M.A., Varoujian, G., Tam, R., 1998, ApJS, 117, 25
- Marco, O., Alloin, D. 2000, A&A, 465, 472
- Marco, O., Alloin, D. 1998, A&A, 336, 823
- Márquez, I., Durret, F., Delgado, R. M. G., Marrero, I., Masegosa,

- J., et al. 1999, *A&AS*, 140, 1
- Martini, P., Regan, M. W., Mulchaey, J. S., Pogge, R. W. 2003, *ApJS*, 146, 353
- Mason, K. O., Branduardi-Raymont, G., Ogle, P. M., Page, M. J., Puchnarewicz, E. M., et al. 2003, *ApJ*, 582, 95
- Mcalary, C.W., McLaren, R.A., Mcgonagal, R.J., Maza, J. 1983, *ApJS* 52, 341
- Molendi, S., Maccacaro, T., Schaeidt, S. 1993, *A&A*, 271, 18
- Molendi, S., Maccacaro, T. 1994, *A&A*, 291, 420
- Moshir, M., Kopan, G., Conrow, T., McCallon, H., Hacking, P., et al. 1990, in *Infrared Astronomical Satellite Catalogs, The faint source catalog, version 2.0*.
- Mulchaey, J. S., Wilson, A. S., Tsvetanov, Z. 1996, *ApJ*, 467, 197
- Nagar, N. M., Oliva, E., Marconi, A., Maiolino, R. 2002, *A&A*, 391, L21
- Nagar, N. M., Wilson, A. S., Mulchaey, J. S., Gallimore, J. F. 1999, *ApJS*, 120, 209
- Nandra, K., George, I. M., Mushotzky, R. F., Turner, T. J., Yaquob, T. 1997, *ApJ*, 477, 602
- Osterbrock, D.E. 1988 *Astrophysics of gaseous nebulae and active galactic nuclei*, University Science Books
- Osterbrock, D.E., Pogge, R.W. 1985, *ApJ*, 297, 166
- Page et al. 2001, *A&A*, 365, L152
- Page, M. J., Carrera, F. J., Mittaz, J. P. D., Mason, K. O. 1999, *MNRAS*, 305, 775
- Penston, M., Fosbury, R. A., Bokseberg, A., Ward, M., Wilson, A. S. 1984, *MNRAS*, 208, 347
- Pogge, R.W., Owen, J.M. 1993, OSU Internal Report 93-01
- Prieto, M. A., Meisenheimer, K., Olivier, M., Reunanen, J., Contini, M., et al. *ApJ*, Accepted. astro-ph/0406620
- Puchnarewicz, E. M., Mason, K. O., Cordova, F. A., Kartje, J., Branduardi-Raymont, G., et al. 1992, *MNRAS*, 256, 589
- Rayner, J.T., Toomey, D. W., Onaka, P. M., Denault, A. J., Stahlberger, W. E., et al. 2003, *PASP*, 155, 362
- Rodríguez-Ardila, M. G. Pastoriza, Viegas, S.M., Sigut, T. A. A., Pradhan, A. K. 2004, *A&A*, in press, astro-ph/0406402
- Rodríguez-Ardila, A., Prieto, A., Viegas, S.M. In Proc. of IAU Symposium No. 222, *The Interplay Among Black Holes, Stars and ISM in Galacti Nuclei*. In press, astro-ph/0406648
- Rodríguez-Ardila, A., Viegas, S.M. 2003, *MNRAS*, 340, 33L
- Rodríguez-Ardila, A., Viegas, S.M., Pastoriza, M.G., Prato, L. 2002a, *ApJ*, 579, 214
- Rodríguez-Ardila, A., Viegas, S.M., Pastoriza, M.G., Prato, L. 2002b, *ApJ*, 565, 140
- Rodríguez-Ardila, A., Viegas, S.M., Pastoriza, M.G., Prato, L., Donzelli, C.J. 2002c, *ApJ*, 572, 94
- Romano, P., Mathur, S., Turner, T. J., Kraemer, S. B., Crenshaw, D. M., et al. 2004, *ApJ*, 602, 635
- Rudy, R. J., Mazuk, S., Puetter, R. C., Hamann, F. 2000, *ApJ*, 539, 166
- Rudy, R. J., Lynch, D. K., Mazuk, S., Venturini, C. C., Puetter, R. C., Hamann, F. 2001, *PASP*, 113, 916
- Rudy, R.J., Levan, P.D., Rodriguez-Espinosa, J.M. 1982 *AJ*, 87, 598
- Sako, M, et al. *ApJ*, 596, 114
- Santos-Lléo, M., Clavel, J., Barr, P., Glass, I., Pelat, D., et al. 1995, *MNRAS*, 274, 1
- Schlegel, D. J., Finkbeiner, D. P., Davis, M. 1998, *ApJ*, 500, 525
- Shemmer, O., Netzer, H. 2002 *ApJ*, 567, L19
- Sigut, T. A. A., Pradhan, A. K. 2003, *ApJS*, 145, 15
- Sigut, T. A. A., Pradhan, A. K. 1998, *ApJ*, 499, L139
- Sosa-Brito, R. M., Tacconi-Garman, L. E., Lehnert, M. D., Gallimore, J. F. 2001, *ApJS*, 136, 61
- Spinoglio, L., Malkan, M.A., Rush, B., Carrasco, L., Recillas-Cruz, E. 1995 *ApJ*, 453, 616
- Stepanian, J. A., Benítez, E., Krongold, Y., Cruz-González, I., de Diego, J. A., Chavushyan, V., Mújica, R., Dultzin-Hacyan, D., Verdugo, T. 2003, *ApJ*, 588, 746
- Thornley, M. D., Schreiber, N. M., F., Lutz, D., Genzel, R., Spoon, H. W. W., Kunze, D., Sternberg, A. 2000, *ApJ*, 539, 641
- Ulvestad, J. S., Antonucci, R. R. J., Goodrich, R. W. 1995, *AJ*, 109, 81
- Vacca, W. D., Cushing, M. C., Rayner, J. T. 2003, *PASP*, 115, 389
- Vaughan, S., Fabian, A. C. 2003, *MNRAS*, 341, 496
- Veilleux, S. 1991, *ApJ*, 369, 331
- Verma, A., Lutz, D., Sturm, E., Sternberg, A., Genzel, R., Vacca, W. 2003, *A&A*, 403, 829
- Véron-Cetty, M.-P.; Véron, P., Gonçalves, A. C. 2001, *A&A*, 372, 730
- Véron-Cetty, M. P., Véron, P. 2000, *A&ARv*, 10, 81
- Viegas, S.M., Contini, M. 1994 *ApJ*, 428, 113
- Walter, R., Fink, H. H. 1993, *A&A*, 274, 105
- Yuan, W., Brinkmann, W., Siebert, J., Voges, W. 1998, *A&A*, 330, 108
- Zombeck, M.V. 1990 in *Handbook of Space Astronomy and Astrophysics* (Cambridge: Cambridge Univ. Press)